Physics in Medicine & Biology

PAPER • OPEN ACCESS

Skin dosimetry in megavoltage radiotherapy using hydrogenated amorphous silicon on a tissue-equivalent flexible substrate

To cite this article: Aishah Bashiri *et al* 2026 *Phys. Med. Biol.* **71** 155020

IOP Publishing Phys. Med. Biol. 71 (2026) 155020 https://doi.org/10.1088/1361-6560/ae8ef6

Physics in Medicine & Biology

PAPER

OPEN ACCESS

RECEIVED
10 March 2026

REVISED
1 June 2026

ACCEPTED FOR PUBLICATION
22 July 2026

PUBLISHED
6 August 2026

Skin dosimetry in megavoltage radiotherapy using hydrogenated amorphous silicon on a tissue-equivalent flexible substrate

Aishah Bashiri[1,2], Cameron Anderson[1], Jessie Posar[1], Shane Pavitt[1], Yashiv Dookie[3], Joanne McNamara[3], Rabia Sandhu[1], Saba Aziz[4,5], Lucio Calcagnile[4,5], Daniela Calvo[6], Domenico Caputo[7,8], Anna Paola Caricato[4,5], Roberto Catalano[9], Massimo Cazzanelli[10], Roberto Cirio[6], Giuseppe Antonio Pablo Cirrone[9], Federico Cittadini[11,12], Tommaso Croci[11,12], Giacomo Cuttone[9], Gianpiero de Cesare[7,8], Paolo de Remigis[6], Sylvain Dunand[13], Michele Fabi[14,15], Luca Frontini[16,17], Catia Grimani[14,15], Mariacristina Guarrera[9], Hamza Hasnaoui[10], Giacomo Insero[15,18], Maria Ionica[11], Keida Kanxheri[11,19], Georgios Konstantinou[13], Francesca Lenta[6,20], Valentino Liberali[16,17], Loris Barraud[13], Nicola Lovecchio[7,8], Marta Ponzecchi[15,18], Giuseppe Maruccio[4,5], Maurizio Martino[4,5], Giovanni Mazza[6], Mauro Menichelli[11], Anna Grazia Monteduro[4,5], Arianna Morozzi[11], Augusto Nascetti[7,21], Stefania Pallotta[15,18], Daniele Passeri[11,23], Maddalena Pedio[11,22], Giada Petringa[9], Francesca Peverini[11,19], Pisana Placidi[11,23], Matteo Polo[10], Alberto Quaranta[10], Gianluca Quarta[4,5], Silvia Rizzato[4,5], Federico Sabbatini[15], Leonello Servoli[11], Alberto Stabile[16,17], Cinzia Talamonti[15,18], Luca Tosti[11], Monica Setia Vasquez Mora[16,17], Alberto Verdini[11,22], Mattia Villani[14,15], Richard James Wheadon[6], Nicolas Wyrsch[13] and Marco Petasecca[1,*]

[1] Centre for Medical Radiation Physics, University of Wollongong, Northfields Ave, Wollongong, NSW 2522, Australia
[2] Department of Physics, Faculty of Arts and Sciences Najran University, King Abdulaziz Rd, Najran 1988, Saudi Arabia
[3] Shoalhaven Cancer Care Centre, Nowra, NSW 2541, Australia
[4] INFN Sezione di Lecce, via per Arnesano, 73100 Lecce, Italy
[5] Department of Mathematics and Physics 'Ennio de Giorgi' University of Salento, Via per Arnesano, 73100 Lecce, Italy
[6] INFN Sez. di Torino Via Pietro Giuria, 1, 10125 Torino, Italy
[7] INFN Sezione di Roma 1, Piazzale Aldo Moro 2, Roma, Italy
[8] Dipartimento Ingegneria de all'informazione, Elettronica e Telecomunicazioni, dell'Università degli studi di Roma via Eudossiana, 18, 00184 Roma, Italy
[9] INFN Laboratori Nazionali del Sud, Via S.Sofia 62, 95123 Catania, Italy
[10] INFN TIFPA c/o Dipartimento di fisica dell'università di Trento, Via Sommarive 14, 38123 Povo, Trento, Italy
[11] INFN, Sez. di Perugia, via Pascoli s.n.c., 06123 Perugia, Italy
[12] Dipartimento di Fisica e Astronomia Università di Padova, via Marzolo 8, 35131 Padova, Italy
[13] Ecole Polytechnique Fédérale de Lausanne (EPFL), Photovoltaics and Thin-Film Electronics Laboratory (PV-Lab), Rue de la Maladière 71b, 2000 Neuchâtel, Switzerland
[14] DiSPeA, Università di Urbino Carlo Bo, 61029 Urbino, PU, Italy
[15] INFN Sezione di Firenze, Via Sansone 1, 50019 Sesto Fiorentino, Firenze, Italy
[16] INFN Sezione di Milano Via Celoria 16, 20133 Milano, Italy
[17] Dipartimento di Fisica dell'università degli Studi di Milano, via Celoria 16, 20133 Milano, Italy
[18] Dipartimento di Scienze Biomediche sperimentali e Cliniche 'Mario Serio', University of Florence, Viale Morgagni 50, 50134 Firenze, FI, Italy
[19] Dip. di Fisica e Geologia dell'università degli Studi di Perugia, via Pascoli s.n.c, 06123 Perugia, Italy
[20] Politecnico di Torino, Corso Duca degli Abruzzi 24, 10129 Torino, Italy
[21] Scuola di Ingegneria Aerospaziale Università degli studi di Roma. Via Salaria 851/881, 00138 Roma, Italy
[22] CNR Istituto Officina dei Materiali (IOM), via Pascoli s.n.c., 06123 Perugia, Italy
[23] Dipartimento di Ingegneria, Università degli Studi di Perugia, via G. Duranti 93, 06125 Perugia, Italy
[*] Author to whom any correspondence should be addressed.

E-mail: marcop@uow.edu.au

Keywords: skin dose, *in vivo* dosimetry, radiotherapy, amorphous silicon, radiation detector

Abstract

Acute skin toxicity after radiation treatments highlights the need for improved dose monitoring and measurement, as the treatment planning system does not accurately estimate skin dose. Wearable radiation detectors may be the solution for most *in vivo* dosimetry needs, but they require innovative materials. The purpose of this work is to overcome the challenges that limit accurate skin dosimetry by exploring the use of hydrogenated amorphous silicon (a-Si:H) fabricated on a flexible polyimide substrate for direct radiation detection. The a-Si:H detector was fabricated on a 125 μm polyimide substrate with a thickness of 3.6–10 μm. The detector's response to the build-up region of the percentage depth dose (PDD) of the MV photon beam was compared to Geant4 radiation transport simulations and benchmarked to Attix ionization chamber measurements. Angular dependency and surface field factors at the phantom surface were compared to Attix IC. The PDD measurement is within 2% of Geant4's simulation and the Attix chamber's response from 150 μ m to 25 mm in a plastic water phantom. All samples showed linear dose responses with 0.37% reproducibility. The a-Si:H device matches the Attix chamber for surface field factor measurements (6–10 MV photon beams, for 5 to 25 cm field sizes). The angular dependence ($-60°$ to $+60°$) compared to the Attix IC confirms the sensor's WED of 150 $\pm$ 5 μm. This study demonstrates that a-Si:H sensors on flexible plastic substrates have a potential for accurate surface dose measurements and agree with reference detectors. This thin, flexible detector provides real time measurements and is stable under high radiation doses. The possibility to assemble with ease an array of a-Si:H pixels over large areas with different sizes and shapes, makes this technology attractive for *in vivo* dosimetry.

1. Introduction

Measurement of *in vivo* superficial dose during radiotherapy has gained increasing significance, particularly with the adoption of advanced treatment techniques that employ high dose rates, multiple tangential beam angles, and highly modulated fields, all of which can elevate superficial dose (Bruand *et al* 2022, Cilla *et al* 2023). Moreover, as the skin is the largest and most exposed organ, and its epithelial tissues provide a critical protective barrier that should be spared from radiation-induced damage, accurate dosimetric assessment is essential to minimize treatment-related toxicities. Several studies reported acute toxicity to the skin after radiotherapy treatments, underscoring the necessity for improved skin dose monitoring and measurement techniques (Bruand *et al* 2022, Cilla *et al* 2023, Malhotra *et al* 2024). The steep dose gradient observed within the first millimetre of the skin, significantly complicates the measurements and represents a challenge that requires the development of specialised techniques and detectors.

Calculating the superficial dose by a treatment planning system (TPS) has been proven to be inaccurate due to limitations in the TPS dose kernel at shallow depths such as dose grid and voxel size as well as difficulties in electron contamination modelling. Large inconsistency has been reported between planned and delivered doses below 10 mm water equivalent depths (WED) (Lv *et al* 2021, Singh Saini *et al* 2021, Hamada *et al* 2024). TPS algorithms are optimised for dose calculations within homogeneous tissues which is not the case for measurements at shallow depths. The accuracy of the skin dose predicted by TPS has been recorded to be $\pm$ 20% (Court *et al* 2008) and deviations of up to 10% has been reported at curved areas and at electron energies ranging from 6 to 12 MeV (Ding *et al* 2005). Thus, validating TPS calculations through real-time skin-dose measurements and monitoring *in vivo* dosimetry with minimal beam perturbation is crucial.

An ideal skin dosimeter should be flexible to conform to body curve surfaces, should have a thin sensitive volume to measure the dose in the build-up region accurately, provide real time measurement, be angular, dose rate and energy independent, and have minimum perturbations of the beam. Ideally a pixelated device would provide more information and facilitate alignment and identification of critical/hot dose spots.

Current flexible dosimeters used clinically to verify the skin dose delivered to the patient during irradiation include Radiochromic films such as EBT3/4 (Santos *et al* 2021), optically stimulated luminescent dosimeters (OSLDs) (Zhuang and Olch 2014, Park *et al* 2017) and Thermoluminescent Dosimeters (TLD, Yukihara *et al* 2022, Khandaker *et al* 2024). They are tissue equivalent with excellent spatial resolution and mechanically flexible materials and angular independent response.

However, these dosimeters cannot provide an instantaneous measurement of the dose, their WED is between 0.15 and 0.8 mm and often accuracy can be affected by the readout performance (optical scanner or reader) or operator handling. They also require pre/post-processing for dose measurement, which is labour-intensive and time-consuming.

The MO*Skin,* recently commercialized by Electrogenics Pty Ltd (MOSkin Dosimetry 2026 Online: https://moskin-dosimetry.com/), is a 350 μ m thick metal-oxide semiconductor field-effect transistors (MOSFETs) sensor. It is a real-time dosimeter used for skin dosimetry with WED of 0.07 mm. It is highly sensitive to the radiation beam with excellent spatial resolution (Kwan *et al* 2008). However, it is also available in single device packaging, has a limited dynamic range (with a maximum accumulated dose of <50 Gy), and its implementation in a 2D array on a flexible substrate would be unrealistic due to high costs (Jong *et al* 2014, Vicoroski *et al* 2017).

Ionization chambers (ICs) are commonly used as a standard tool in radiotherapy for calibration and quality assurance (QA) due to their energy and dose rate response independence in addition to their high reproducibility. The Attix IC (Model 449 CNMC Co. Nashville, TN—USA) is a parallel plate IC and has proven to be a reliable surface dosimeter with an electrode made of a thin plastic window (Kwan *et al* 2008). This entrance window electrode is made of Kapton and is 0.025 mm thick with a 2 mm gap from the opposite electrode plate. It has a large guard-ring of 13.5 mm diameter, which reduces the overresponse observed in unguarded parallel plate ICs caused by lateral leakage currents. However, its design, size and mechanical rigidity are limiting factors for use in *in vivo* applications and for measurements of field sizes smaller than 5 $\times$ 5 cm^2.

Fibre optic dosimeters are also a valuable alternative for *in vivo* surface dosimetry (Guang *et al* 2025). They provide tissue equivalence in most radiation fields used in radiotherapy and they can be organized in arrays. Despite these advantages, they can be affected by Cherenkov light generated in the optical fibre during irradiation, which may degrade spatial resolution and reduce dosimetric accuracy if not properly corrected. Additionally, the use of plastic scintillators increases the overall thickness of the detector, leading to a greater WED and potentially decreasing the device's flexibility to detect dose at sub millimetric depths.

To compensate the limitations of commercially available dosimeters, a bolus may be used in some clinics to accurately define the WED and estimate dose *in-vivo* by establishing an electronic equilibrium, however, this practice increases skin toxicity by shifting the maximum dose toward the surface of the skin.

Several flexible skin dosimeters have recently been investigated as *in vivo* dosimeters for curved structures (Cho *et al* 2020). Cho *et al* developed a flexible film dosimeter by coating a radiochromic-sensitive film with a flexible silicone rubber material to maintain the flexibility of the film resulting in a total thickness of 0.80 mm. The measured dose with these films to planned dose variation was found to be between −0.1% and 1.2% for four patients plans (2020). However, this dosimeter does not provide real time measurements, and its WED has not been validated to quantify the skin dose. Han *et al* fabricated flexible photoconductor dosimeters by mixing monoxide materials (lead oxide (PbO) and mercury oxide (HgO)) with silicone rubber binder to investigate their potential use as surface dosimeters in electron therapy. They demonstrated excellent linearity and reproducibility of 1.5% and minimal dose-rate dependence (2021). However, their capability to measure dose at depths below 1 mm, as well as their surface angular dependence, has not been verified.

Other research groups are exploring the potential of using photovoltaic based diodes as skin dosimeters as they can be fabricated with thin layers on flexible substrates and can be readout in real-time. A thin-film photodiode system was developed by using eight amorphous silicon (a-Si) solar cells, each with an active area of 1.5 $\times$ 5.0 cm^2 and a total thickness of 200 μm (Zygmanski *et al* 2014). The dosimetric characteristics of the system shows promising results. However, it has low efficiency, which may limit its ability to detect radiation at low dose rates, such as in the condition of skin dose measurements. Another study attempted to address the issue of low efficiency by utilizing a 2 $\times$ 2 cm^2 scintillator with a thickness of 1 mm. However, the thickness of the system with this configuration still does not match the performance of other commercially available skin dosimeters, such as EBT3 film and MO*Skin* (Jeong *et al* 2023). Moreover, copper indium gallium selenide solar cells have been studied as flexible, real-time skin dosimeters for electron radiation therapy (Shin *et al* 2023). These devices offer excellent linear dose response and are cost-effective. However, bending the dosimeter beyond a 10 mm curvature radius causes permanent damage and signal loss. They have a total thickness of 0.33 mm and are built on a stainless-steel sheet, which is a non-water-equivalent substrate, potentially affecting beam fluence and creating strong secondary electron contamination. Additionally, the dosimeter exhibits only partial angular independence, with signal reductions up to 16% for tangential beams, and its surface angular dependence has not yet been assessed.

Overall, there remains no available detector technology that combines thin and flexible array formats with stable dose-accumulation response and real-time readout while maintaining negligible angular, energy, and dose-rate dependence for reliable surface dosimetry.

In this work, we introduce the hydrogenated amorphous silicon (a-Si:H) detectors, developed within the Hydrogenated Amorphous Silicon Pixels Detectors (HASPIDE) collaboration (2022b, Menichelli *et al* 2022c). These devices have proved to be radiation hard and to have the ability to be deposited on flexible substrates for applications in photon, electron and proton beam dosimetry, profile monitoring, neutron detection, and space applications (Menichelli *et al* 2022b, Large *et al* 2023).

The a-Si:H based detectors have recently been characterized for applications in therapeutic x-ray beams and they have demonstrated a comparable performance to commercially available dosimeters (Menichelli *et al* 2024). Characterization was performed to demonstrate their suitability as a machine QA tool at the maximum dose depth. Excellent performance at the depth of maximum dose does not demonstrate that a dosimeter is valid for skin measurements, because the skin-relevant region lies much closer to the surface where the dose gradient, scatter conditions, and charged particle equilibrium are substantially different. A true skin dosimeter must therefore be validated specifically under superficial-dose conditions, since accuracy at depth cannot be assumed to translate to accuracy at or near the surface.

This work aims to verify that a-Si:H detectors can be effective as a skin dosimeter at the surface of a water equivalent phantom, where Charged Particle Equilibrium is absent, and a steep dose gradient exists in the buildup region.

In order to provide a truly mechanically flexible device, the a-Si:H detectors adopted for this study have been deposited on a 125 μm thick polyimide substrate, providing a response variation within 3% even at curvature radii as small as 7 mm, therefore allowing the device to conform to various anatomical superficial shape of the body (Large *et al* 2024). The flexibility aims to enhance the accuracy in skin dose measurements by eliminating air gaps between the device and curved areas of the body.

2. Materials and methods

2.1. Device structure

The a-Si:H detectors in this experiment were manufactured by the PV-Lab at École Polytechnique Fédérale de Lausanne (EPFL), Neuchâtel, Switzerland. They were developed in two distinct configurations: NIP diodes and charge-selective contact devices (CSC). The NIP diodes consist of a stack of a thin film (tens of nm) of p-doped a-Si:H, a thicker layer (between 1 and 10 μm) of intrinsic a-Si:H, and a thin layer of n-type doped a-Si:H. The back contact is a stack of Cr/Al/Cr and the top electric transparent contact is Indium Zirconium Oxide (IZrO).

The CSC devices follow a three-layer structure, including a thin film of metal oxide, where hole mobility exceeds electron mobility, made of Molybdenum oxide (MoOx), a 3.6 μm layer of intrinsic a-Si:H, and a thin layer of a metal oxide where electron mobility is greater than hole mobility, fabricated either with Titanium dioxide (TiO_2) or Aluminium-doped Zinc Oxide (AZO).

The a-Si:H is deposited by the Plasma-Enhanced Chemical Vapour Deposition (PECVD) technique, at a temperature ranging from 250 to 300 °C using a mixture of Silane (SiH_4) and hydrogen, on a mechanically flexible polyimide (Kapton) substrate with 125 μm thickness (Menichelli *et al* 2022a, 2024). Each sensor consists of either 2 × 3 or 3 × 3 arrays of 5 × 5 mm^2 pixels with 1 mm edge-to-edge distance. The response of sensors with smaller pixels area of 2 × 2 mm^2 were also investigated.

The sensor is connected to a 35 cm long flexible Kapton strip and electrically bonded by a carbon-based conductive paint (MG Chemicals 838AR), which is mechanically secured to the sensor surface by a dual compound epoxy glue. In order to isolate the sensor from environmental light, they have been covered with a film darkened by graphite-based paint. Figure 1 shows the structure and mechanical flexibility of the devices tested in this work.

The real-time readout measurement of all pixels is performed by connecting the tail into a multichannel electrometer developed in-house by the Centre of Medical Radiation Physics (University of Wollongong, Australia).

2.2. Physical characterization

2.2.1. Leakage current and temperature dependence

A measure of the leakage current as a function of applied reverse bias in the range of ± 1 V was performed using a Keithley 2636B source measure unit (SMU) under dark conditions. The measurements were performed on samples with different configuration structure and thicknesses. This was carried out to assess both the quality of the samples' substrate, the electrical bonding quality by the carbon-based paint and to determine the relevant range of voltages to operate the diodes. These preliminary characterizations are essential steps toward the development of a detector suitable for *in vivo* dosimetry.

A relative detector must be calibrated with respect to a reference detector in order to determine the dose. The calibration is often performed in a phantom at reference conditions at a temperature oscillating around a standard room temperature of 25 °C. The calibration factors obtained in this condition may be affected by placing the detector on the skin of the patient at temperature varying from 35 to 40 °C. In order to assess the variations of baseline current and sensitivity of the detector as a function

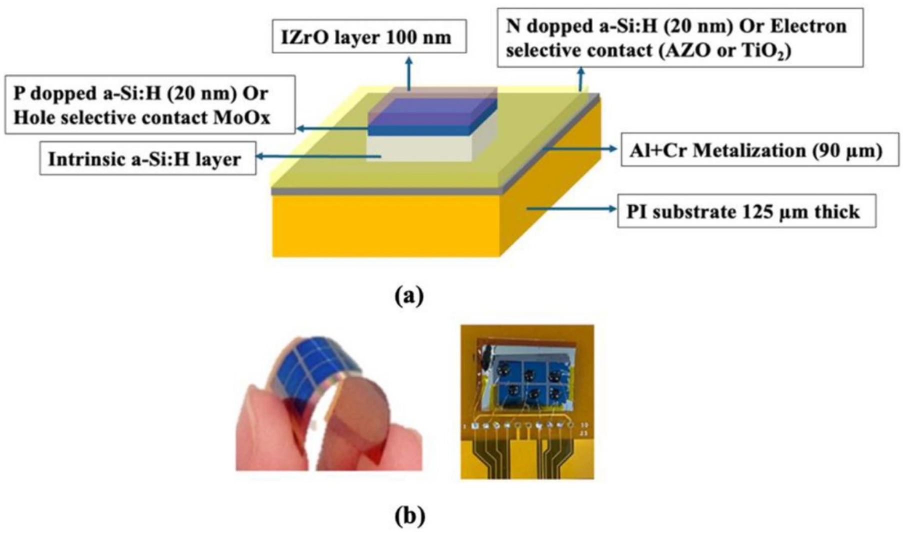

Figure 1. (a). Illustrates the structure of the amorphous silicon detectors, while (b). Shows the flexibility of the device and the electrical connection of the pixels.

of temperature, the photocurrent response of the sensors has been tested inside a thermal chamber and the temperature was controlled with a Thermoelectric Temperature Controller (Thermoelectric, model TC-720) and stabilized within ±1 °C. The photocurrent of the a-Si:H were measured using the SMU by increasing the temperature from 20 °C to 45 °C, at 0.28 V μm^{-1}.

2.2.2. External quantum efficiency (EQE)

The EQE was carried out by a commercial EQE system (PV Measurement, model QEX10) in order to evaluate the effect caused by variations of substrate thickness and bias applied to the diodes. The photocurrent signals were calibrated and normalized against a standard silicon photodiode. This setup evaluates spectral response and photon-to-electron conversion efficiency by utilizing a xenon arc lamp, a monochromator, filters, and reflective optics under controlled bias and lighting conditions.

The monochromatic light beam, covering an area of 1 cm^{-2}, was focused on the diode's centre. Photocurrent was recorded across wavelengths from 300 to 900 nm in 10 nm steps for diodes with thicknesses varying between 1 and 10 μm under passive mode and with negative bias ranging from −0.5 V to −3 V. EQE helps to identify the quality of the substrate-contact interface, charge generation and recombination effects and the efficacy of the electric field generated by the external bias. These parameters are essential in order to select the best substrate thickness/contact-type for a surface dosimeter.

2.3. Dosimetry for therapeutic MV x-ray beams

The irradiation of the sensors was performed by using a linear accelerator (LINAC) Varian Clinac 21iX at the Shoalhaven Cancer Care Centre (SCCC) in Nowra (NSW, Australia). All measurements, unless specified otherwise, were performed by delivering a total of 100 MU at a nominal rate of 600 MU min^{-1} using 6 MV photon beams, and pulse rate of 360 Hz, corresponding to an instantaneous dose of 2.78×10^{-4} Gy/pulse under reference conditions (Field size of 10×10 cm ^{2}, Source to Surface distance of 100 cm and depth placed at 1.5 cm in a water equivalent phantom). The radiation was aligned to the central diode of the a-Si:H detector within a 10 × 10 cm^2 field, collimated by open-field jaw and using a Flattening Filtered photon beam, with a source-to-surface distance (SSD) of 100 cm. The response of the a-Si:H diode in this study is the average of three repetition of each measurement and the uncertainty was calculated by one standard deviation over these repetitions.

2.3.1. Linearity and calibration factors

Dose linearity was obtained at the maximum depth dose ($d_{\max} = 1.5$ cm) of a 6 MV photon beam in solid water. The responses of the a-Si:H sensors were recorded from 10 cGy to 200 cGy for devices with different thicknesses (3.6, 4, 5, 7.5 and 10 μm).

Calibration factors for signal-to-dose conversion of the a-Si:H diodes were calculated as the inverse of the slope of the linear fit of the obtained readings and expressed in cGy/pC; the resulting sensitivity (expressed in pC/cGy) was plotted as a function of the diode thickness.

2.3.2. Percentage depth dose (PDD)

A PDD curve was obtained using the CSC a-Si:H diode with AZO as a back contact and the Attix IC (Model 449 CNMC Co. Nashville, TN USA) and compared to the Geant4 simulation for both 6 and 10 MV photon beams. The thickness of the solid water phantom above the detector was varied from 0.15 mm to 1 mm, in steps of 0.15 mm, by introducing films of water equivalent plastic above the detector while maintaining the nominal value of SSD at 100 cm with 10 cm of backscatter. Beyond the WED of 1 mm, increments of 2 mm have been added up to 25 mm adjusting the position of the phantom to maintain the SSD to 100 cm at each step.

Monte Carlo simulations for expected PDD profile were calculated by Geant4 version 10.0.01 using the blueprint of the Linac 21iX head provided by Varian, precisely replicating the experimental conditions of irradiation in a $30 \times 30 \times 30$ cm^3 water phantom and by a 10×10 cm^2 x-ray field at 100 cm SSD (Vicoroski *et al* 2017). The physics models were built based on the Geant4 Electromagnetic Standard Physics package, accounting for photoelectric effect, Compton scattering, gamma conversion, ionization, Bremsstrahlung, and positron annihilation. Both the particle range cut, and the electron/positron maximum step length were set to 0.1 mm, and dose was scored using a voxel size of $0.02 \times 1 \times 1$ mm^3. The mean dose and its standard deviation were recorded based on 10 simulations. A total of 4×10^{13} primary electron histories were simulated, resulting in a dose uncertainty of around 0.5% at 1.5 cm depth on the central axis for 10×10 cm^2 field. This simulation model has already been validated on a previous study (Oborn *et al* 2014).

The PDD curve calculated by Geant4 has been validated using the Attix chamber and then adopted to estimate the effective WED of the aSi:H detector.

The surface dosimetry using the CSC a-Si:H diode, with AZO as a back contact, has been carried out by placing the detector on the surface of 10 cm thick, 30×30 cm^2 solid water phantom using 6 MV and 10 MV photon beam within a 10×10 cm^2 field and SSD of 100 cm. The error bars measured as the standard deviation based on three measurements.

2.3.3. Surface field factor

The surface field factor was assessed by determining the responses of a-Si:H sensors to a 100 cGy dose, with radiation field sizes ranging from 5×5 to 25×25 cm^2 under 6 and 10 MV photon beams. The measurements for each field size were normalized to the measurement at 10×10 cm^2 and compared with the results obtained from the Attix IC under identical conditions. The surface factor of the Attix IC was also evaluated by increasing the WED of the Attix IC to be 0.15 mm using a 90 μm polyimide sheet placed on top of the detector to explore the effect of variation of the effective WED of the detector.

2.3.4. Angular dependence

To estimate the surface angular dependence of the a-Si:H sensor for photon beams, the detector response to 100 cGy was evaluated at various gantry angles from $-60°$ to $60°$ in $15°$ increments. The response was then normalized to the normal incidence direction at $0°$ angles. The results were compared to the data obtained from the Attix IC for 6 and 10 MV photon beam.

3. Results

3.1. Physical characterization

3.1.1. Leakage current and temperature dependence

Figure 2 illustrates the leakage current in relation to the applied bias. The dark current shows a clear rectification effect, showing that the CSC and NIP devices are functioning as diodes with an exponentially increasing current after a bias voltage of 0.2 V. However, among the other diodes tested, CSC_TiO_2 exhibits the lowest leakage current, approximately -0.05 pA at -0.4 V, while CSC_AZO exhibits a leakage current about eight times higher at the same bias level.

Figure 3 depicts how the CSC diode response varies with temperature for diodes with a 3.6 μm thick layer and TiO_2 and AZO back contacts, operated at a voltage of -0.28 V μm^{-1}. The leakage current was normalized to its measurement at 25 °C. Both devices show a comparable linear increase in photocurrent across the temperature range. Although the devices have the same thickness, they exhibit different temperature dependencies, and this variation increases under applied bias compared to operation in passive mode. In TiO_2-based diodes, increasing the temperature from 25 °C to 40 °C results in a response increase of under 4%, whereas the AZO device shows an approximately 8% variation over the same range.

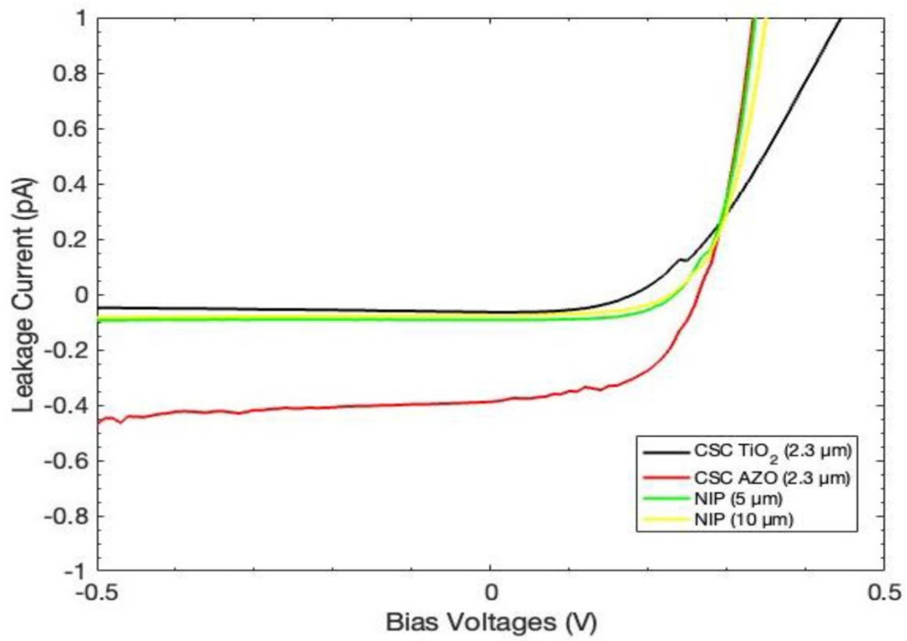

Figure 2. Reverse leakage current measurements of various a-Si:H diodes having different structures and thicknesses for pixels of 5×5 cm^2 size. According to the Keithley 2636B SMU, current is recorded with an accuracy of ± 0.1 fA in the range of bias ± 1 V and current ± 200 pA.

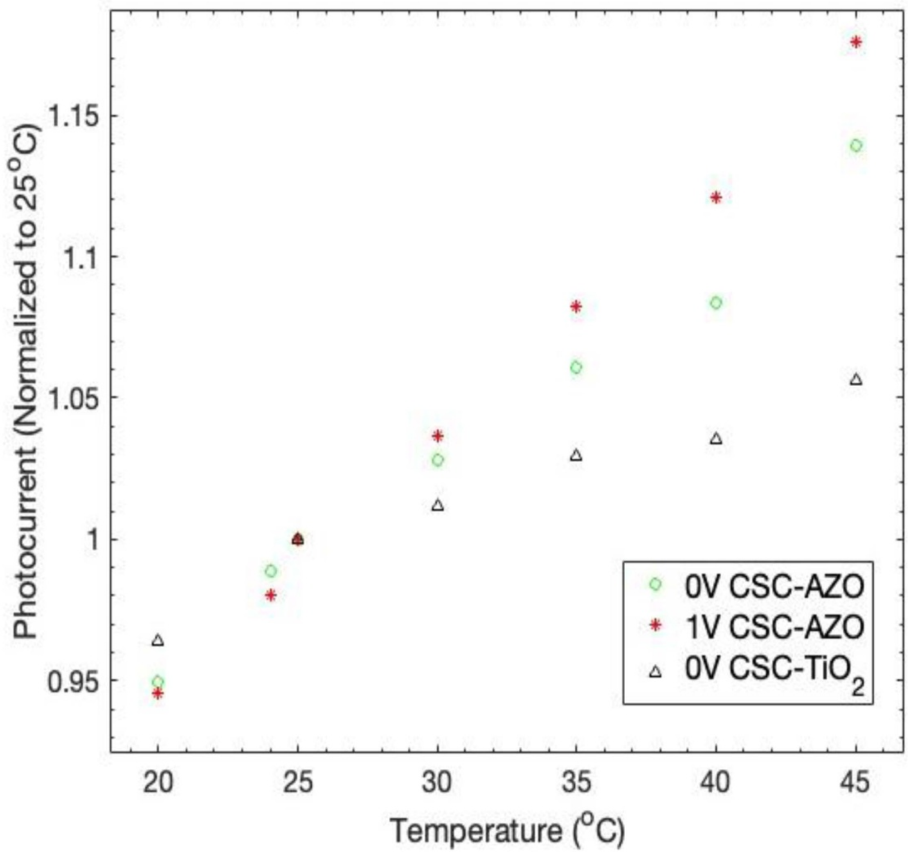

Figure 3. Displays the photocurrent as a function of temperature normalized to the response at 25 °C for CSC diodes with a thickness of 3.6 μm and pixel area of 5×5 cm^2, operated at bias of -0.28 V μm^{-1} as well as at passive mode. The temperature is stabilized within ± 1 °C. and the accuracy of current measurements with Keithley 2636B SMU with ± 0.1 fA resolution.

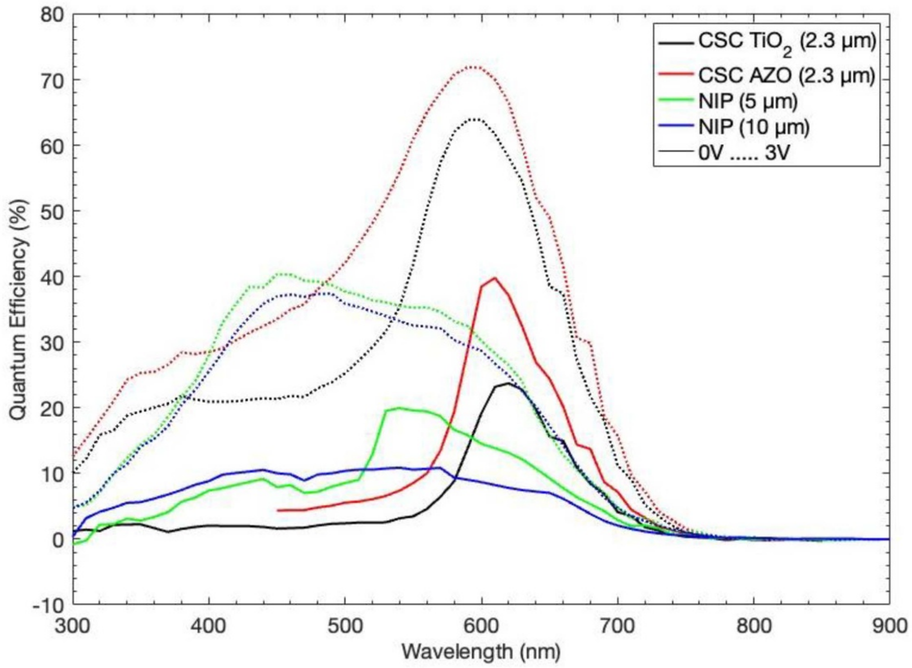

Figure 4. External quantum efficiency for diodes with various thicknesses and structures (CSC and NIP), the result displayed for measurements operated at 0 V and −3 V. EQE was measured with a PV Measurements QEX10. According to system specifications, the absolute EQE uncertainty is approximately ±1% and with wavelength uncertainty of ±2 nm at room temperature.

3.1.2. EQE

Figure 4 presents the EQE measurements for diodes of different thicknesses and structures (CSC and NIP), recorded on passive mode and under reverse bias conditions of 3 V. When operated on passive mode, the EQE is lower for diodes with larger thicknesses. However, applying a bias voltage enhances the EQE. Additionally, a systematic higher efficiency is observed in CSC in respect to NIP structures. Under reverse bias, CSC TiO_2 presents a higher EQE increase (threefold) than CSC AZO (twofold). NIP devices show a higher EQE at shorter wavelengths proving the doped junction contacts to allow for higher penetration and charge collection underneath the contacts. This is an important feature for a detector for surface dosimetry which requires a thin sensitive volume in order to mimic a shallow water equivalent depth.

3.2. Dosimetry for therapeutic x-ray beams

3.2.1. Linearity

Figure 5 illustrates the linear response of charge collection by a-Si:H sensors with various structural configurations and thicknesses across a dose range of 10–300 cGy. Linearity was confirmed for nearly all diodes, with a coefficient of determination $R^2 = 0.999$. However, the sensor featuring a 4 μm thick active layer exhibited reduced linearity ($R^2 = 0.935$) when operated in passive mode, this is likely to be due to the outlier point. This response improved significantly under a −1.2 V bias, achieving $R^2 = 0.999$. Data for the 10 μm thick device under bias is not shown in the figure because the data acquisition system saturated.

Table 1 summarizes the dose calibration factors which are used to convert collected charge to absorbed dose, derived from the gradient of the linear plots. While NIP sensors demonstrate higher sensitivity relative to thicker sensors with smaller active areas (2×2 mm^2), this trend does not hold for devices with larger pixel dimensions. Notably, sensitivity improves with increasing sensor thickness under applied bias as shown in figure 6. There is a direct proportionality of sensitivity to area, but it does not scale linearly with thickness of the sensor. Sensors based on the CSC architecture demonstrated both enhanced sensitivity and excellent linearity. Furthermore, devices utilizing AZO as the back contact layer exhibit superior sensitivity to photon beam.

The 10 μm thick device operated under bias condition exhibited a response that exceeded the dynamic range of the data acquisition system; therefore, the measurements were not recorded.

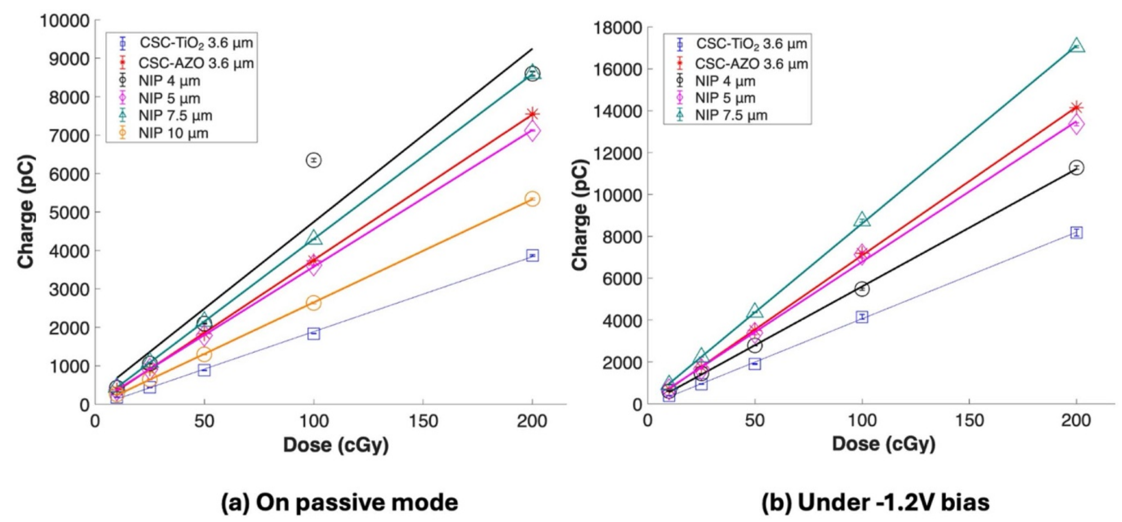

Figure 5. Illustrates the linear response of charge collection by a-Si:H sensors with various structural configurations and thicknesses for pixels with area of 5 × 5 cm^2. (a. on passive mode, b. under −1.2 V bias). The linear fit for measurements with 4 μm thickness device under passive mode (black line) is affected by the outlier point at 100 cGys. Error bars represent one standard deviation over three repetitions and are contained within the marker size.

Table 1. Summarizes the dose calibration factors/sensitivity of a-Si:H diodes calculated as the gradient of the linear plots.

		Sensitivity at 0 V (pC/cGy)		Sensitivity at −1.2 V (pC/cGy)	
Sensor	Thickness (μm)	5×5 (mm^2)	2×2 (mm^2)	5×5 (mm^2)	2×2 (mm^2)
NIP	4	45± 7	—	56.1± 0.6	—
	5	35.44± 0.09	6.664± 0.012	66.5± 0.8	13.2± 0.5
	7.5	42.59± 0.12	8.52± 0.03	83.7± 0.5	17.06± 0.07
	10	26.73±0.06	10.14± 0.07	DAQ saturated.	20.47± 0.18
CSC_TiO_2	3.6	19.5± 0.3		41.4± 0.5	
CSC_AZO	3.6	37.84± 0.17		70.9± 0.5	

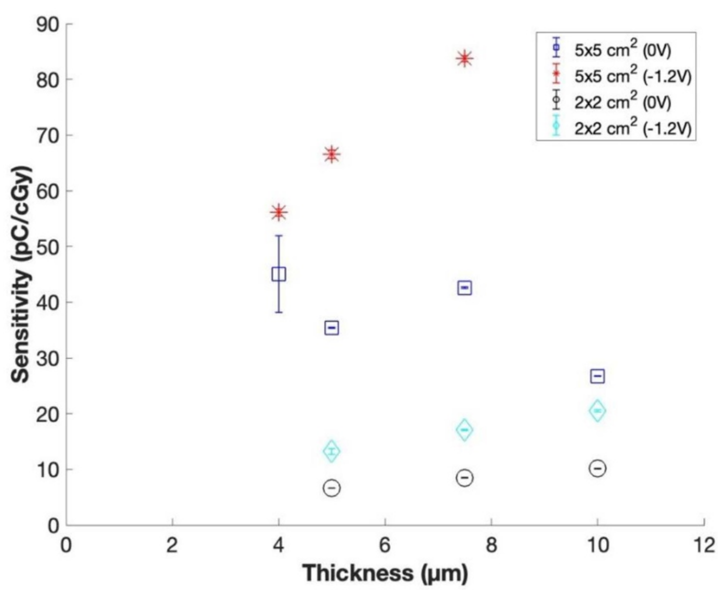

Figure 6. The effect of area and thickness on the NIP diodes' sensitivity to therapeutic x-ray Beams. Error bars represent one standard deviation between repeated measurements. The NIP diode with 4 µm thickness shows large baseline fluctuation in passive mode resulting in larger error bars. This is also confirmed by the linear fit in figure 4, which shows a less linear response.

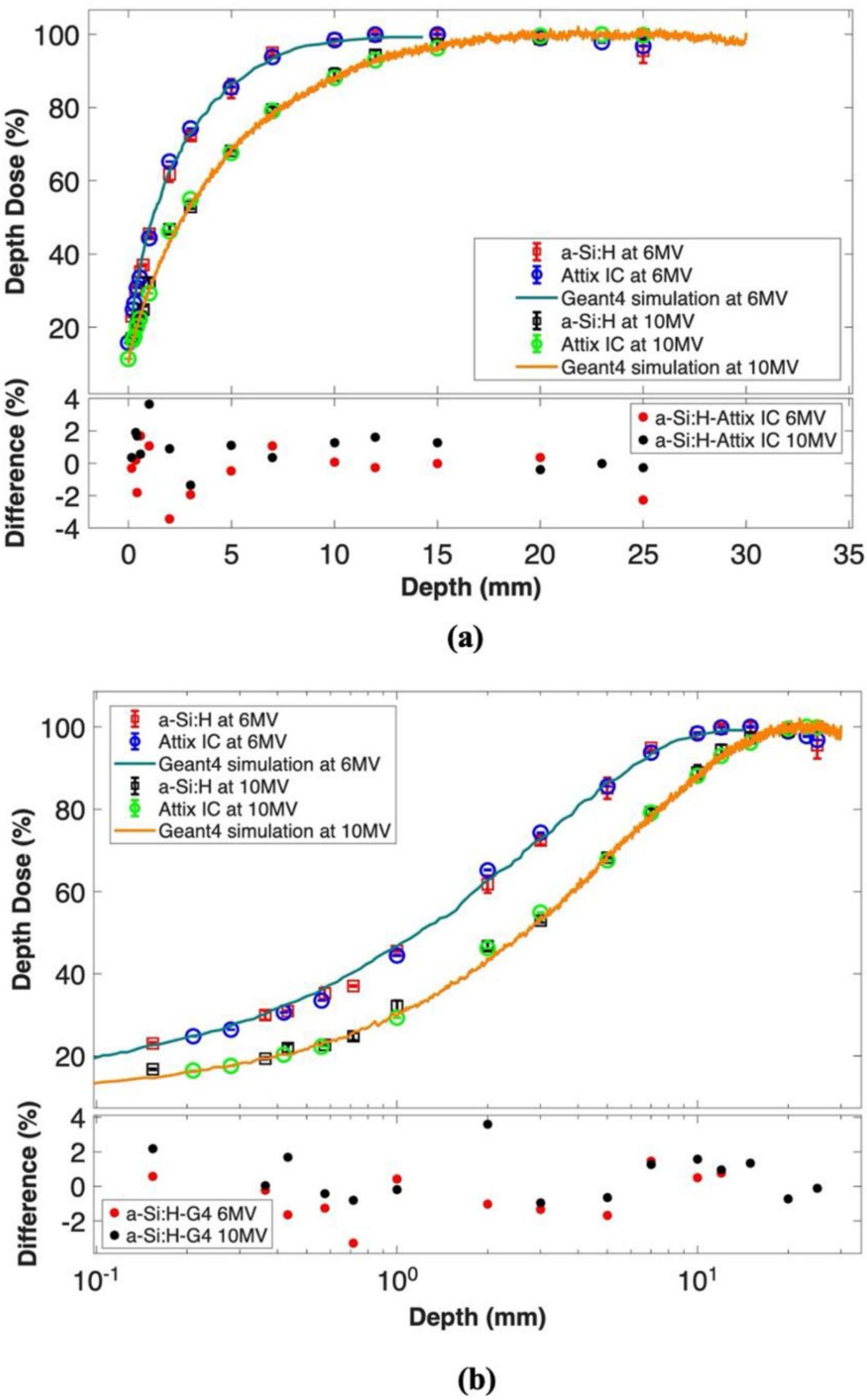

Figure 7. (a) A percentage depth dose measurements obtained using an a-Si:H array and the Attix ionization chamber for photon beams of 6 MV and 10 MV compared with Geant4 simulation. (b) The same measured datasets plotted in a logarithmic scale. Error bars represent one standard deviation over three repetitions.

3.2.2. PDD

Figure 7 shows the comparison between measurements taken with a-Si:H diodes, the Attix IC and data obtained by Geant4 at various depths in solid water. Measurements are all normalized at depth corresponding to $d_{\max}$ (15 mm for 6 MV and 23 mm for 10 MV photon beams), under a radiation field of 10×10 cm^2.

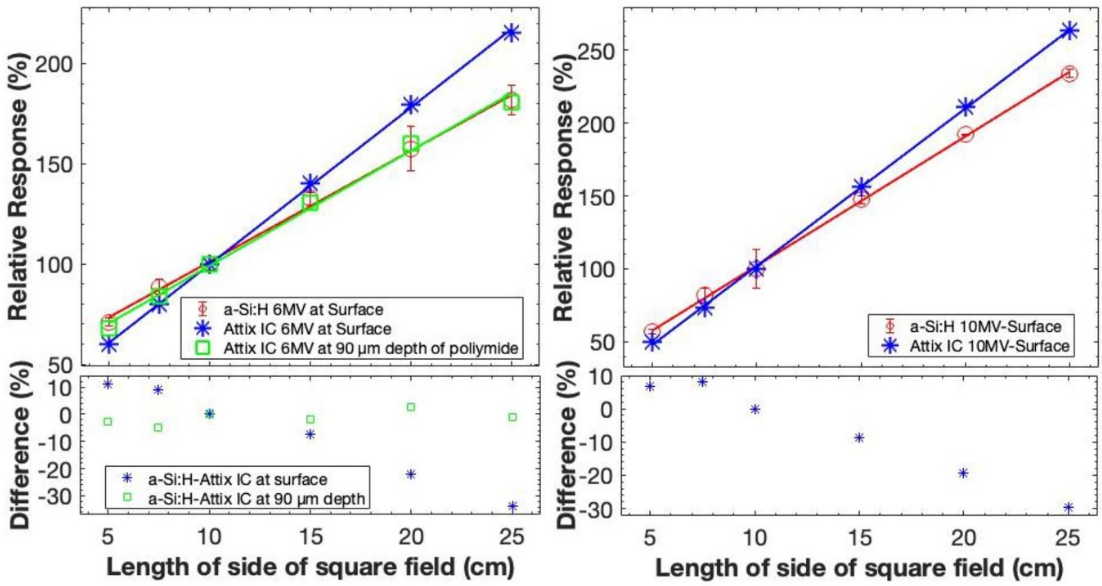

Figure 8. Comparison of field-size dependence between the a-Si:H positioned at the surface of a water phantom and Attix chambers with varying build-up thicknesses using 6 (left) and 10 MV (right) photon beam. Error bars represent one standard deviation over three repetitions.

The PDD measured by the aSi:H diodes at 'surface' position, aligns with the simulation data when the sensor is at a WED of approximately 150 $\pm$ 5 μ m. The WED of the aSi:H arises from the combination of the darkened thick film used to make the detector light tight and the overlayer created by the epoxy glue used to create the electrical contact. This result is also validated by the estimation of the WED of the Attix IC when compared to Geant4 simulations which corresponds to approximately 30 $\pm$ 5 μm, as expected.

PDD demonstrates an agreement between a-Si:H diode and Attix IC measurements within 2% across the whole phantom for 6 MV photon beam except at 2 mm water equivalent, where a maximum deviation of 3.4% was observed. In the case of 10 MV photon beam, agreement holds within 1%, apart from an outlining overresponse of 3.6% recorded at 1 mm WED.

Furthermore, the comparison between experimental diode measurements and Geant4 simulations indicated discrepancies within 2% for both 6 MV and 10 MV photon beam with only two outliers at 1 mm WED of 3.4% and 3.6% for 6 MV and 10 MV photon beams, respectively. These results highlight a consistent correlation between measured and simulated data.

3.2.3. Field factor

Figure 8 presents surface dose measurements obtained using the a-Si:H detector and the Attix IC at various field sizes. Measurements at each field size are normalized to the response recorded at a 10 $\times$ 10 cm^2 field and are benchmarked against the response of the Attix IC.

The results indicate that the aSi:H diode can reconstruct correctly the linear behaviour expected for a field factor at surface in MV photon beam energies. The Attix chamber produced a steeper gradient as a function of the lateral field size because of its thinner WED in comparison to the aSi:H diodes. This is confirmed by the data obtained using the Attix chamber with an overlayer of 90 μm of polyimide (approximately a WED of 120 μm) that matches the Field Factor measured by the diodes with a discrepancy within 1.3% for field sizes between 5 and 25 cm^{-2}.

3.2.4. Angular dependence

The angular dependence of superficial dose measurements obtained using the a-Si:H diode, normalized to the measurement at a gantry angle of 0°, is compared to Attix chamber's in figure 9. The findings indicate that by placing the dosimeter at the surface of the phantom, the superficial dose increased with beam incidence angles leading to higher doses.

The PRIMO Monte Carlo simulations, reported by Mahur *et al* (2022), indicate that the superficial dose at surface for a beam incident at 60° is approximately twofold higher than that for normal incidence (0°). The Attix IC's response shows a lower response in respect to the theoretical value calculated

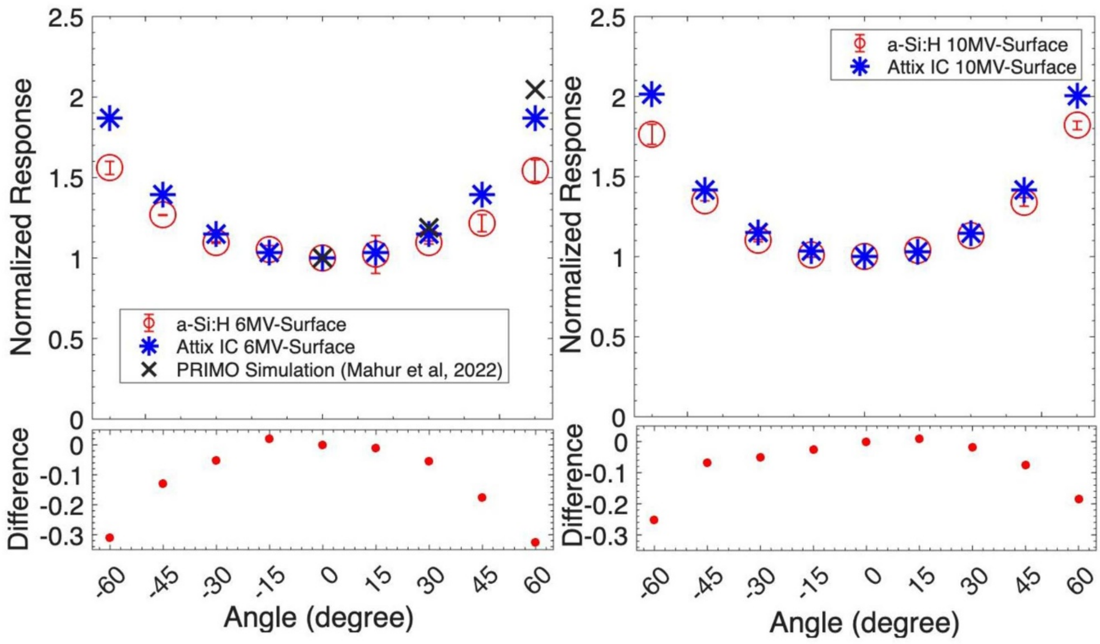

Figure 9. Evaluation of the normalized angular response of a-Si:H diodes and an Attix ionization chamber at the surface of a solid water phantom for 6 MV (left) and 10 MV (right) photon beams. Left figure also shows the PRIMO Monte Carlo simulation at 0 depth for 6 MV photon beam (Mahur *et al* 2022). Error bars representing one standard deviation over three repetitions.

by the simulations as it does not calculate the dose at zero depth but rather at its point of measurement, which is located below the surface. Comparative analysis of the experimental results shows that the response of the a-Si:H detectors is lower than that of the Attix IC for incident angles larger than 30° for the 6 MV beam. These results suggest that the equivalent point of measurement of the a-Si:H detector is located at deeper depth than that of the Attix IC. Nevertheless, the a-Si:H detector was still able to reproduce the angular dependence expected for superficial dose measurements.

4. Discussion

The measurement of leakage current versus voltage has been carried out to select the combination of contact technology (NIP or CSC) and thickness of the substrate which maximise sensitivity and minimise the fluctuation of the current baseline for the dosimeter adopted for skin dosimetry. All the tested devices show relatively low leakage currents, but CSC devices excel with minimal baseline amplitude and high stability. The increase in photocurrent with temperature indicates that the mobility within the a-Si:H diode increases with increasing temperature mainly because carriers spend less time trapped in localized (band-tail) states at higher temperature. In a study of charge transport in amorphous silicon, the measured current can be strongly influenced by the carrier mobility according to $\mu = A^* V^m T^n \exp\left(b\frac{\sqrt{|F|}}{T}\right)$, where V is the internal electrostatic potential, A^* and b are fitting parameters, and F is the electric field (Passeri *et al* 2024). The exponents m and n characterize the sensitivity of mobility to potential and temperature, respectively. In this representation, the mobility is a combination of linear dependence and exponential term trap field-assisted transport. When operating the device with low bias (-0.28 V μm^{-1} in this study), the exponential contribution becomes negligible at low temperatures, whereas the linear component has comparatively greater influence as shown in figure 3.

The results also show that this behaviour depends on both the contact type and the mode of operation. This determines whether these variations require correction or can be considered negligible. This needs to be taken into consideration if the detector is used for *in vivo* dosimetry as the temperature of the patient is likely to result in overestimation of the radiation dose in respect to the conditions of calibration.

Based on these results, it is recommended that the skin dosimeter be fabricated with TiO_2 as the back contact, since it exhibits lower temperature dependence, and that the diode be operated in passive mode. For accurate *in vivo* dosimetry, a correction for temperature variation is required.

The temperature correction k_T is determined empirically by giving the same known dose at the reference temperature and at the treatment temperature, then taking the ratio of the two readings:

$$k_T = \frac{M_{T_{\text{ref}}}}{M_{T_{\text{treat}}}}$$

where $M_{T_{ref}}$ is the measurement under reference (calibration) condition and $M_{T_{\text{treat}}}$ is the measurement at treatment temperature. The treatment reading is then corrected by multiplying it by the correction factor.

EQE decreases with diode thickness which is likely due to reduced charge collection efficiency caused by charge trapping over the longer travel distances of optical photons in thicker devices. In contrast, an increase of the EQE is observed when a bias voltage is applied: the internal electric field improves charge collection and reduces effects of recombination. The CSC TiO_2 diode exhibits a greater EQE increase with applied bias but its charge collection efficiency at 0 V is very inefficient proving to be a suboptimal contact type for passive use, whereas the CSC AZO diode conserves better charge extraction and sensitivity under passive operation, making it more suitable for clinical applications. This observation may be attributed to the respective work functions of AZO and TiO_2, which lie in the ranges of 4.2–4.35 eV and 4.5–6.8 eV, respectively. These values indicate a more favourable alignment between the work function of AZO and that of the Al electrode ($\sim$4.2 eV). Consequently, the electron injection/extraction barrier is reduced, which decreases contact losses and enhances charge collection.

The detectors exhibited dose linearity across a range of different thicknesses and active areas. NIP-type sensors proved to be sub-optimal candidate for a skin dosimeter. Although small pixel proved to be more stable and consistent, the sensitivity of either small or large diodes did not scale with thickness of the active layer. Applying bias created large variation of the leakage current in NIP diodes, making them unsuitable for measurements of small amplitude dose rates such as the ones detected at surface.

The saturation of the data acquisition system observed for the 10 μm-thick devices under bias is attributable to both limitations of the readout system dynamic range and the high leakage current arising from the thicker intrinsic layer of the diode. These limitations should not affect the clinical applications as the detector is intended to be used in passive mode.

Comparative analysis of both detector configurations (NIP and CSC) revealed that the CSC architecture achieved superior sensitivity and lower dark currents. The selective contacts facilitated efficient carrier extraction, suppressed charge recombination, and minimized dark current, resulting in a device with superior sensitivity.

Simulations and comparison with Attix IC of the PDD show that the aSi:H sensor has a WED of approximately 0.15 mm. The accuracy of skin dosimetry measurements at shallow depths is greatly influenced by the thickness of the sensor's sensitive volume and its relative position in respect to the steep dose gradient at the surface of a water equivalent phantom. Although the sensitive volume of the a-Si:H diode itself is only 3.6 μm thick, the overall WED is defined primarily by the bonding technique and packaging employed for the sensor assembly. Specifically, graphite conductive paint and epoxy have been applied over the diode pads, followed by an encapsulation in a 70 μm polyimide sheet darkened with a graphite loaded paint. These additional layers, cumulatively, result in the effective WED of 0.15 mm for the sensor. However, the a-Si:H diode measurements agreed within 2% with both the Geant4 simulation and the Attix IC measurements for doses measured at depths ranging from 150 μm to 25 mm in a plastic water phantom.

The packaging adopted allows the sensor to be flexible and adhere to any curved surface such as the patients' body. However, The WED could be reduced and match the ICRP recommendation for skin dosimetry, but a more sophisticated bonding technique must be developed to maintain the mechanical flexibility of the sensor.

Measurements at the surface of the phantom confirmed that the a-Si:H detector is able to reproduce the expected linear trend of the field factor at the surface of a phantom (Apipunyasopon *et al* 2013). The comparison of the response obtained by the diodes with the Attix chamber measurements using an overlayer of 120 μm WED, confirmed the WED of approx. 150 μm within 1.3%.

The a-Si:H diode reproduces also the angular dependence expected for dose measurements at a phantom surface as demonstrated by comparison with the experimental data obtained by the Attix IC and the theoretical data obtain by PRIMO-MC simulations. In fact, the dose of a MV photon beam is expected to increase with the beam's angle of incidence due to the shift of d_{max} toward the surface. This occurs because the path length inside the phantom becomes longer as electrons travel along an oblique trajectory, where the effective path length to reach d_{max} is given by $L = d_{\text{max}}/\cos\theta$, with θ representing the beam angle in respect to the normal direction to the surface of the phantom. This angular dependence is more significant for 6 MV photon beams due to their shallower buildup region compared to 10 MV beams.

The expected surface angular response is illustrated in figure 9, showing the same overall trend observed in the detector measurements and confirming that both detectors effectively measure dose at depths slightly beneath the 'true' surface. For a beam delivered at 60°, the ideal response would be approximately twice that measured under perpendicular irradiation. In this study, the Attix IC, with a WED of 0.03 mm, showed a 1.9-fold increase relative to its response at 0°, while the a-Si:H diode, with a WED of 0.15 mm, showed an increase of 1.6-fold. Although the a-Si:H diode is considered angularly independent, it still demonstrated a 10% difference compared with the Attix chamber, most likely due to the difference on WED between the two detectors. This result is particularly important for treatments involving oblique beam delivery, as it identifies WED as a critical parameter in skin dosimetry. It also highlights a limitation of the current a-Si:H detector design and bonding technique, demonstrating that even a thin encapsulation layer can introduce substantial variation in the measured surface dose.

5. Conclusion

This study demonstrated the development and evaluation of flexible hydrogenated amorphous silicon detectors for surface dosimetry in megavoltage radiotherapy. The results showed good agreement between the a-Si:H diode and the Attix IC for MV photon beams across field sizes from 5 to 25 cm, supporting the feasibility of this technology for real-time *in vivo* dosimetry. The angular dependence measurements indicated that the depth of effective measurement of the a-Si:H diode is greater than that of the Attix chamber, which lead to non-negligible underestimation of the dose at beam incidence angles of and greater than 45°. Nevertheless, these findings highlight the strong potential of the detector for incorporation into high-radiation-tolerant 2D dosimetric arrays.

A key challenge for future development is the reduction of the WED of the diode to meet the ICRP recommendation for skin dose measurement at 75 μm. Achieving this objective is possible and requires tailored adjustments to the diode connection technology and encapsulation, specifically intended for accurate skin dosimetry. As this study was limited to open-field irradiations on flat phantom surfaces, further work is required to evaluate detector performance under modulated beam delivery and on curved anatomical surfaces.

Acknowledgment

The authors would like to thank the Shoalhaven Cancer Care Centre (SCCC) staff for their valued time and assistance with measurements. A Bashiri is funded by the Deanship of Graduate Studies and Scientific Research at Najran University under the SAFEER Funding Program grant code (NU/SAFEER/SERC/14/381-1). This work was conducted as part of the INFN HASPIDE project.

Data availability statement

The data cannot be made publicly available upon publication because they are not available in a format that is sufficiently accessible or reusable by other researchers. The data that support the findings of this study are available upon reasonable request from the authors.

Author contributions

Aishah Bashiri 0000-0003-3273-9435
Conceptualization (lead), Data curation (lead), Formal analysis (lead), Methodology (lead), Software (lead), Visualization (lead), Writing – original draft (lead), Writing – review & editing (lead)

Cameron Anderson
Conceptualization (supporting), Data curation (supporting), Investigation (supporting)

Jessie Posar
Writing – review & editing (equal)

Shane Pavitt 0009-0003-3845-5481
Data curation (equal), Formal analysis (equal)

Yashiv Dookie
Methodology (supporting), Resources (supporting), Writing – review & editing (equal)

Joanne McNamara
Methodology (supporting), Resources (supporting), Writing – review & editing (equal)

Rabia Sandhu 0009-0002-5844-6876
Data curation (supporting), Formal analysis (supporting), Methodology (supporting)

Saba Aziz
Writing – review & editing (equal)

Lucio Calcagnile
Writing – review & editing (equal)

Daniela Calvo
Writing – review & editing (equal)

Domenico Caputo
Writing – review & editing (equal)

Anna Paola Caricato
Writing – review & editing (equal)

Roberto Catalano
Writing – review & editing (equal)

Massimo Cazzanelli 0000-0002-3182-5908
Writing – review & editing (equal)

Roberto Cirio
Writing – review & editing (equal)

Giuseppe Antonio Pablo Cirrone
Writing – review & editing (equal)

Federico Cittadini
Writing – review & editing (equal)

Tommaso Croci
Writing – review & editing (equal)

Giacomo Cuttone
Writing – review & editing (equal)

Gianpiero de Cesare
Writing – review & editing (equal)

Paolo de Remigis
Writing – review & editing (equal)

Sylvain Dunand
Writing – review & editing (equal)

Michele Fabi 0000-0002-2464-1369
Writing – review & editing (equal)

Luca Frontini 0000-0002-1137-8629
Writing – review & editing (equal)

Catia Grimani 0000-0002-5467-6386
Writing – review & editing (equal)

Mariacristina Guarrera
Writing – review & editing (equal)

Hamza Hasnaoui 0009-0003-1293-3588
Writing – review & editing (equal)

Giacomo Insero 0000-0003-0992-2434
Writing – review & editing (equal)

Maria Ionica
Writing – review & editing (equal)

Keida Kanxheri
Writing – review & editing (equal)

Georgios Konstantinou
Writing – review & editing (equal)

Francesca Lenta
Writing – review & editing (equal)

Valentino Liberali 0000-0003-1333-6876
Writing – review & editing (equal)

Loris Barraud 0009-0008-6150-628X
Writing – review & editing (equal)

Nicola Lovecchio
Writing – review & editing (equal)

Marta Ponzecchi
Writing – review & editing (equal)

Giuseppe Maruccio 0000-0001-7669-0253
Writing – review & editing (equal)

Maurizio Martino
Writing – review & editing (equal)

Giovanni Mazza 0000-0003-3174-542X
Writing – review & editing (equal)

Mauro Menichelli
Writing – review & editing (equal)

Anna Grazia Monteduro
Writing – review & editing (equal)

Arianna Morozzi
Writing – review & editing (equal)

Augusto Nascetti
Writing – review & editing (equal)

Stefania Pallotta 0000-0003-4123-7971
Writing – review & editing (equal)

Daniele Passeri
Writing – review & editing (equal)

Maddalena Pedio 0000-0002-3305-4318
Writing – review & editing (equal)

Giada Petringa
Writing – review & editing (equal)

Francesca Peverini
Writing – review & editing (equal)

Pisana Placidi
Writing – review & editing (equal)

Matteo Polo
Writing – review & editing (equal)

Alberto Quaranta
Writing – review & editing (equal)

Gianluca Quarta
Writing – review & editing (equal)

Silvia Rizzato 0000-0002-3908-4796
Writing – review & editing (equal)

Federico Sabbatini
Writing – review & editing (equal)

Leonello Servoli
Writing – review & editing (equal)

Alberto Stabile
Writing – review & editing (equal)

Cinzia Talamonti 0000-0003-2955-6451
Writing – review & editing (equal)

Luca Tosti
Writing – review & editing (equal)

Monica Setia Vasquez Mora
Writing – review & editing (equal)

Alberto Verdini 0000-0001-8880-2080
Writing – review & editing (equal)

Mattia Villani
Writing – review & editing (equal)

Richard James Wheadon
Writing – review & editing (equal)

Nicolas Wyrsch 0000-0002-4588-0166
Writing – review & editing (equal)

Marco Petasecca 0000-0001-5958-7457
Conceptualization (lead), Methodology (lead), Project administration (lead), Supervision (lead), Writing – review & editing (lead)

References

Apipunyasopon L, Srisatit S and Phaisangittisakul N 2013 Equivalent square formula for determining the surface dose of rectangular field from 6 MV therapeutic photon beam *J. Appl. Clin. Med. Phys.* **14** 196–204

Bruand M *et al* 2022 Acute skin toxicity of conventional fractionated versus hypofractionated radiotherapy in breast cancer patients receiving regional node irradiation: the real-life prospective multicenter HYPOBREAST cohort *BMC Cancer* **22** 1318

Cho J D, Son J, Sung J, Choi C H, Kim J S, Wu H G, Park J M and Jin K 2020 Flexible film dosimeter for *in vivo* dosimetry *Med. Phys.* **47** 3204–13

Cilla S *et al* 2023 Machine-learning prediction model for acute skin toxicity after breast radiation therapy using spectrophotometry *Front. Oncol.* **12** 1044358

Court L E, Tishler R B, Allen A M, Xiang H, Makrigiorgos M and Chin L 2008 Experimental evaluation of the accuracy of skin dose calculation for a commercial treatment planning system *J. Appl. Clin. Med. Phys.* **9** 29–35

Ding G X, Cygler J E, Yu C W, Kalach N I and Daskalov G 2005 A comparison of electron beam dose calculation accuracy between treatment planning systems using either a pencil beam or a Monte Carlo algorithm *Int. J. Radiat. Oncol. Biol. Phys.* **63** 622–33

Guang Z, He C, Bry V, Le A, DeMarco J and Chetty I J 2025 Optical fiber sensing technologies in radiation therapy *Photonics* **12** 1058

Hamada K, Fujibuchi T and Arakawa H 2024 Optimum delineation of skin structure for dose calculation with the linear Boltzmann transport equation algorithm in radiotherapy treatment planning *Radiol. Phys. Technol.* **17** 938–46

Han M J, Yang S W, Bae S I, Moon Y M, Jeon W, Choi C W, Park S K and Kim J Y 2021 Evaluation of monoxide film-based dosimeters for surface dose detection in electron therapy *PLoS One* **16** e0251441

Jeong S, An S, Kwon Y C, Pak S I, Cheon W, Shin D, Lim Y K, Jeong J H, Kim H and Lee S B 2023 Development of a real-time *in vivo* dosimetry tool for electron beam therapy using a flexible thin film solar cell coated with scintillator powder *Med. Phys.* **50** 557–69

Jong W L, Hsiu J, Wong D, Ung N M, Ng K H, Ho G F, Cutajar D L and Rosenfeld A B 2014 Characterization of MOSkin detector for *in vivo* skin dose measurement during megavoltage radiotherapy *J. Appl. Clin. Med. Phys.* **15** 120–32

Khandaker M U, Taheri A and Bradley D A 2024 A systematic review on the silica fibre thermoluminescence dosimeters for medical applications *J. Radioanal. Nucl. Chem.* **333** 1507–30

Kwan I S *et al* 2008 Skin dosimetry with new MOSFET detectors *Radiat. Meas.* **43** 929–32

Large M J *et al* 2024 Characterization of a flexible a-Si:H detector for *in vivo* dosimetry in therapeutic x-ray beams *Med. Phys.* **51** 4489–503

Large M J *et al* 2023 Hydrogenated amorphous silicon high flux x-ray detectors for synchrotron microbeam radiation therapy *Phys. Med. Biol.* **68** 135010
Lv R, Yang G, Huang Y and Wang Y 2021 Dosimetric effects of supine immobilization devices on the skin in intensity-modulated radiation therapy for breast cancer: a retrospective study *BMC Cancer* **21** 404
Mahur M, Singh M, Gurjar O P and Semwal M K 2022 Assessment of surface and build-up doses for a 6 MV photon beam using parallel plate chamber, EBT3 gafchromic films, and PRIMO monte carlo simulation code *J. Biomed. Phys. Eng.* **12** 455–64
Malhotra A, Carpentier E E, Grahame S, Chan E K, Nichol A and Duzenli C 2024 Toward a skin dose-area metric predictive of moist desquamation using *in vivo* skin dosimetry and skin assessments *Adv. Radiat. Oncol.* **9** 101318
Menichelli M *et al* 2024 Characterization of hydrogenated amorphous silicon sensors on polyimide flexible substrate *IEEE Sens. J.* **24** 12466–71
Menichelli M *et al* 2022a Testing of planar hydrogenated amorphous silicon sensors with charge selective contacts for the construction of 3D-detectors *J. Instrum.* **17** C03033
Menichelli M *et al* 2022b Development of thin hydrogenated amorphous silicon detectors on a flexible substrate (arXiv:2211.17114)
Menichelli M, Servoli L and Wyrsch N 2022c Status and perspectives of hydrogenated amorphous silicon detectors for MIP detection and beam flux measurements *Front. Phys.* **10** 943306
Oborn B M, Williams M, Bailey M and Carolan M G 2014 IMRT treatment monitor unit verification using absolute calibrated BEAMnrc and Geant4 Monte Carlo simulations *J. Phys: Conf. Ser.* **489** 012020
Park S Y, Choi C H, Park J M, Chun M, Han J H and Kim J 2017 Sensitivity and stability of optically stimulated luminescence dosimeters with filled deep electron/hole traps under pre-irradiation and bleaching conditions *Phys. Medica* **38** 81–87
Passeri D *et al* 2024 TCAD modelling of a-Si:H devices for particle detection applications *Mater. Sci. Semicond. Process.* **169** 107870
Santos T, Ventura T and Lopes M D C 2021 A review on radiochromic film dosimetry for dose verification in high energy photon beams *Radiat. Phys. Chem.* **179** 109217
Shin D S, Kim T H, Rah J E, Lee S B, Lim Y K, Jeong J, Kim H, Shin D and Son J 2023 Flexible real-time skin dosimeter based on a thin-film copper indium gallium selenide solar cell for electron radiation therapy *Med. Phys.* **50** 2402–16
Singh Saini A, Das I J, Hwang C S, Biagioli M C and Lee W E 2021 Skin dose in radiation treatment of the left breast: analysis in the context of prone versus supine treatment technique *Phys. Medica* **81** 114–20
Vicoroski N *et al* 2017 Development of a silicon diode detector for skin dosimetry in radiotherapy *Med. Phys.* **44** 5402–12
Yukihara E G, McKeever S W S, Andersen C E, Bos A J J, Bailiff I K, Yoshimura E M, Sawakuchi G O, Bossin L and Christensen J B 2022 Luminescence dosimetry *Nat. Rev. Methods Primers* **2** 8
Zhuang A H and Olch A J 2014 Validation of OSLD and a treatment planning system for surface dose determination in IMRT treatments *Med. Phys.* **41** 081720
Zygmanski P, Abkai C, Han Z, Shulevich Y, Menichelli D and Hesser J 2014 Low-cost flexible thin-film detector for medical dosimetry applications *J. Appl. Clin. Med. Phys.* **15** 311–26